Cell Reports
Physical Science

CellPress
OPEN ACCESS

Article

Tough Nature-Inspired Helicoidal Composites with Printing-Induced Voids

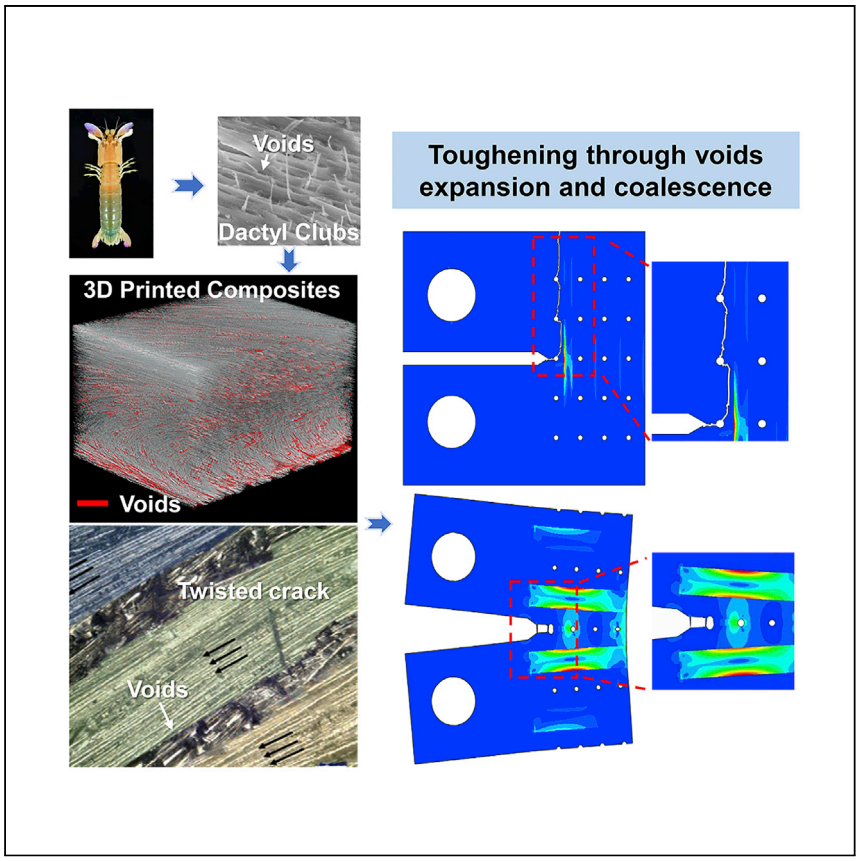

Micro-scale voids are discovered in the exoskeletons of *Odontodactylus japonica*. Yin et al. print bioinspired composites to mimic this material, which are found to have superior specific impact energy in the presence of voids. Simulations indicate that the voids expand and coalesce on loading, contributing to impact toughness.

Sha Yin, Haoyu Chen, Ruiheng Yang, ..., Yiu-Wing Mai, Jun Xu, Robert O. Ritchie

shayin@buaa.edu.cn (S.Y.)
jun.xu@uncc.edu (J.X.)
ritchie@berkeley.edu (R.O.R.)

HIGHLIGHTS

Micron-scale voids are observed adjacent to the Bouligand structures in mantis shrimp

Bioinspired composites are printed to mimic Bouligand architectures with voids

The impact energy of the printed composites is enhanced by the presence of the voids

FEA modeling shows that voids expand and guide twisting cracks to enhance toughness

Yin et al., Cell Reports Physical Science *1*, 100109
July 22, 2020
https://doi.org/10.1016/j.xcrp.2020.100109

Cell Reports
Physical Science

CellPress
OPEN ACCESS

Article

Tough Nature-Inspired Helicoidal Composites with Printing-Induced Voids

Sha Yin,[1,*] Haoyu Chen,[1] Ruiheng Yang,[1] Qinghao He,[2] Dianhao Chen,[1] Lin Ye,[2] Yiu-Wing Mai,[2] Jun Xu,[3,*] and Robert O. Ritchie[4,5,*]

SUMMARY

Exoskeletons of *Odontodactylus japonicas*, the "smasher-type" mantis shrimp, feature a raptorial appendage comprising a Bouligand architecture of chitin nanofibrils with newly observed voids or defects between the polysaccharide α-chitin and protein interfaces. Here, we use a continuous-fiber 3D printing technology to simulate such materials in carbon fiber-reinforced (helicoidal) composites, complete with the presence of voids due to imperfect printing. The specific impact energies of the 3D printed helicoidal composites are clearly superior and further enhanced by the presence of the voids. To explain the role of the Bouligand architecture, interlaminar stresses are computed and found to yield anti-delamination characteristics, and a theoretical model is derived to evaluate the optimal helicoidal architecture. Finite element modeling indicates that the voids tend to deform and coalesce on loading and appear to guide the fracture into the formation of an ideally twisted crack in the printed helicoidal composites, thereby contributing to the impact toughness.

INTRODUCTION

Biological materials invariably feature complex hierarchical microstructures that can exhibit excellent mechanical properties. As an example, during millions of years of evolution, some crustaceans have developed extremely strong, stiff, and tough exoskeletons to resist attack[1] and weapons to engage in attack.[2] The stomatopod dactyl club of the "smasher-type" mantis shrimp, for instance, can impose intensive impact loads of >10 kg at a speed of 23 m/s without generating structural failure.[3] To accomplish this feat, the structure of the appendage comprises three primary regions, each with a distinct architecture—the impact, periodic, and striated regions.[4–6] Of interest to the present study, the periodic region normally consists of a Bouligand-type (twisted plywood) structure[7] of helicoidal laminated chitin fibers embedded in protein matrix, which serves as a major energy-absorption structure during impact.[5,6,8] Weaver et al.[7] investigated the fracture mechanisms across the periodic region of the dactyl club of the stomatopods after impact and found that cracks predominantly grew in a twisted penetrating mode (helicoidal pattern) via fracture of the chitinous organic matrix rather than breaking the fibers; such marked crack deflection and, more important, twisting created by the Bouligand structure induces considerable (extrinsic) toughening and high impact resistance. Considerable effort has been made to understand the basic mechanisms that underlie the exceptional toughness and damage resistance of these bioinspired materials, such as minimizing the crack driving force,[9] maximizing the damage area per unit volume,[10] and increasing the complexity of crack configurations.[11] Theoretical studies

[1]Vehicle Energy & Safety Laboratory (VESL), Department of Automotive Engineering, School of Transportation Science & Engineering, Beihang University, Beijing 100191, China

[2]Centre for Advanced Materials Technology, School of Aerospace, Mechanical, and Mechatronic Engineering, The University of Sydney, Sydney 2006, NSW, Australia

[3]Vehicle Energy & Safety Laboratory (VESL), North Carolina Motorsports and Automotive Research Center, Department of Mechanical Engineering and Engineering Science, The University of North Carolina at Charlotte, Charlotte, NC 28223, USA

[4]Department of Materials Science & Engineering, University of California, Berkeley, Berkeley, CA 94720, USA

[5]Lead Contact

*Correspondence: shayin@buaa.edu.cn (S.Y.), jun.xu@uncc.edu (J.X.), ritchie@berkeley.edu (R.O.R.)

https://doi.org/10.1016/j.xcrp.2020.100109

of the crack driving force for a twisted crack in a Bouligand composite have demonstrated that the resistance to cracking is significantly increased for a twisted crack path compared to a linear (flat) crack in a homogeneous material.[12,13] However, biological materials are a hierarchical assembly of architectures at multiple length scales; their elegant and effective toughening mechanisms are thus complex. Physics-based models to explain the toughening mechanisms are far from complete, which hinders systematic bioinspired designs for possible engineering applications.

The question that we pose in this study is whether the remarkable impact resistance of the mantis shrimp's dactyl club is associated with toughening mechanisms other than those resulting from the Bouligand-type architecture and whether these features can be made and realistically built into synthetic materials to make energy-absorbing structures. To emulate these structures requires the fabrication of synthetic materials that can mimic these structures and mechanisms. This is a challenging task, particularly with respect to finding an appropriate processing method to fabricate nature's complex structures. Although many advanced fabrication techniques are available now,[14] most are "top-down," in which one starts with a large piece of material and then processes it to a smaller scale. Nature's design, however, is "bottom-up," in which the initial atomistic or molecular design is built up over multiple length scales into a macro-scale material. While still an immature process from the perspective of guaranteeing the quality (rather than just the shape) of fabricated components, additive manufacturing represents a promising array of techniques to make bioinspired materials in the image of nature. Biomimetic helicoidal composite materials have been three-dimensionally (3D) printed with hard-soft bi-materials, liquid-crystal polymers, and cement-based materials so as to explore their resulting mechanical properties.[15–18] Also, thin-ply Bouligand composites with a small inter-ply angle have been fabricated using automated tow or tape placement, with the aim of exploring whether enhanced impact damage resistance can be obtained in Bouligand architectures with carbon fiber (CF)-reinforced plastics.[19] Similarly, continuous-fiber reinforced composites can be easily fabricated through fused deposition molding (FDM)-based 3D printing for any type of fiber stacking architecture. In addition, voids as manufacturing defects can be derived either from gas bubbles by volume expansion of moisture or gaps of adjacent filaments during fiber printing, as illustrated by Blok et al.[20] and He et al.[21] Due to their generally deleterious effects on mechanical properties, efforts are invariably made to suppress voids in modern manufacturing techniques, such as with out-of-autoclave curing.[22] However, the plastic growth of voids, which are induced during injection molding in deformed polyamide and polypropylene matrices, have been found to trigger large plastic deformation of the surrounding matrix, which suggests that the presence of voids could play a role in contributing to the toughness.[23,24] However, the effects of such voids on the mechanical properties of bioinspired materials fabricated by additive manufacturing have yet to be investigated.

Dactyl clubs from *Odontodactylus japonicas*, a species of aggressive mantis shrimp with a hammer-like appendage, were targeted in the present study. Morphologies across the transverse section of the periodic region, these appendages were observed and are shown in Figure 1A. Chitin fibers were found to be helicoidally arranged in a Bouligand-type structure with each layer rotated by a small angle α from the layer below, which was consistent with the architecture previously reported for the peacock mantis shrimp (*O. scyllarus*).[7,12,13] However, a different feature was visible, showing the presence of numerous voids randomly distributed with elliptical shapes in the coronal section of the periodic region (Figure 1A), which we believe may have been overlooked in previous studies.

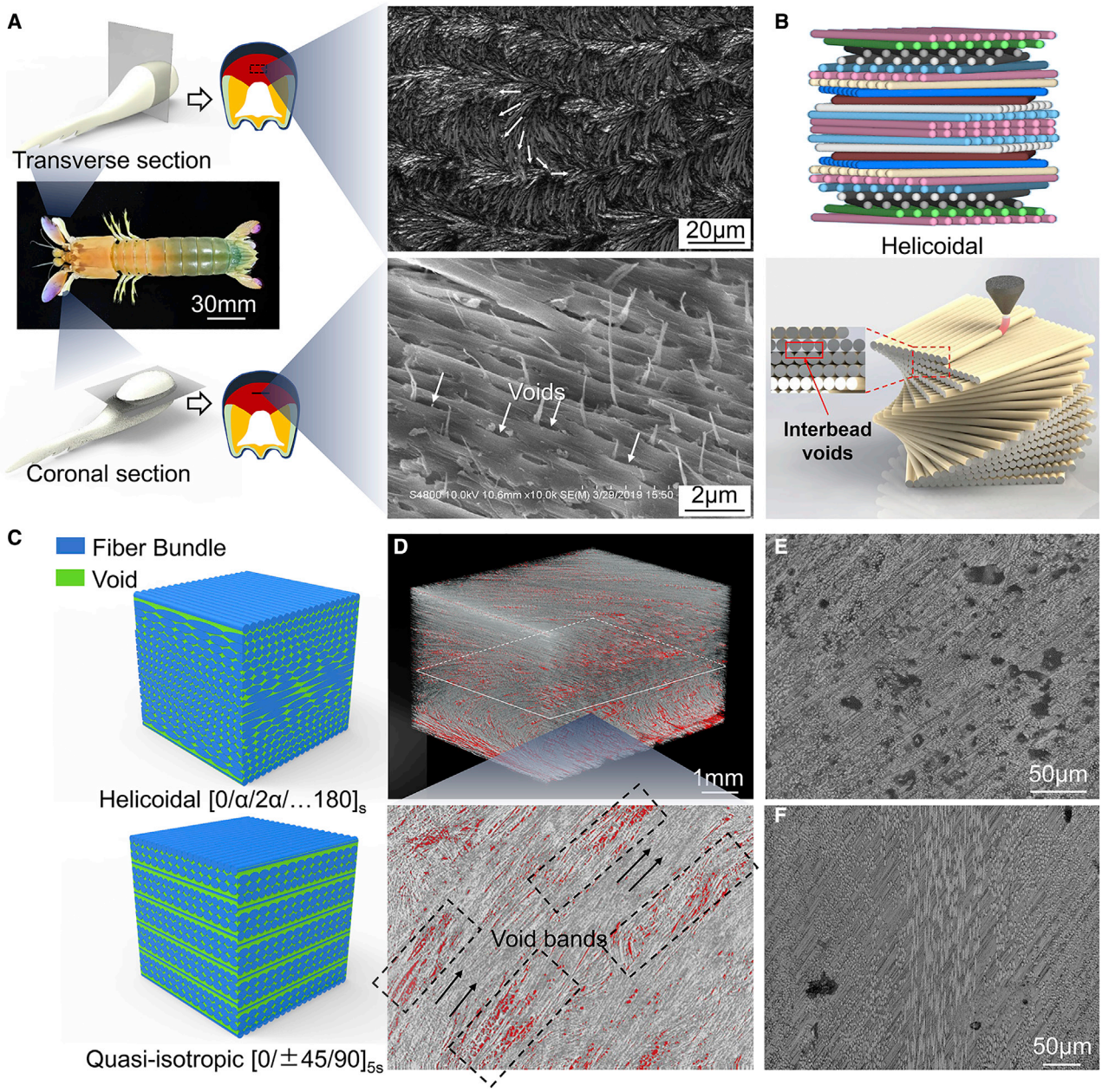

Figure 1. Characterization of Structures

(A) Morphologies of *Odontodactylus japonicas*: SEM images of cross-section and coronal section in periodic region (red).

(B–F) Bioinspired composite laminates created by 3D printing.

(B) Schematic of the helicoidal fiber orientation in the bioinspired composites and the printing process.

(C) Schematic illustration of the ideally distribution pattern of voids in the printed helicoidal composites.

(D) 3D micro-CT image and a sectional view of helicoidal composites by 3D printing showing void distribution marked in red.

(E and F) Micrographs of voids in the polished sections of the helicoidal composites by 3D printing: (E) without hot pressing and (F) with hot pressing.

To mimic the microstructure of the dactyl club, in this work bioinspired helicoidal composite laminates are fabricated using FDM-based 3D printing methods with continuous CFs. All of the printed samples together with the fabrication defects are carefully characterized and then tested in three-point bending and under Charpy pendulum impact loading, with the toughening mechanisms including the Bouligand-type architecture and voids carefully examined. The interlaminar stress

Table 1. Summary of Fabricated Samples with Different Stacking Sequences for Different Tests

Group	Test Method	Specimen Geometry	Stacking Sequence	Dimension (mm)/ Number of Layers
A	Three-point bending	A-1 (Helicoidal 16.36°)	$[0/16.36/32.72\ldots/163.6/180]_S$	(96 ×× 13 × 3.5)/24
		A-2 (Quasi-isotropic)	$[0/\pm45/90]_{3S}$	(96 × 13 × 3.5)/24
		A-3 (Helicoidal 36°)	$[0/36/\ldots/144/180]_S$	(96 × 13 × 3.5)/24
B	Charpy pendulum	B-1 (Helicoidal 9.47°)	$[0/9.47/18.95\ldots/170.53/180]_S$	(80 × 10 × 5.0)/40
		B-2 (Quasi-isotropic)	$[0/\pm45/90]_{5S}$	(80 × 10 × 5.0)/40
		B-3 (Helicoidal 9.47° with hot pressing)	$[0/9.47/18.95\ldots/170.53/180]_S$	(80 × 10 × 4.4)/40

variation within the Bouligand-type structure is analyzed based on our simulation results, and a theoretical model established to correlate the crack growth patterns with the laminate architecture to discern the optimal design for maximum fracture resistance. Furthermore, the role of the voids in fiber composites containing matrix cracks under load is also investigated by finite element (FE) modeling to validate their possible contribution to the toughening.

RESULTS AND DISCUSSION

Microstructural Characterization

Based on the observations of biological microstructures, we designed our synthetic composites with a helicoidal fiber stacking sequence shown in Figure 1B; the helicoidal angle in the laminates was defined as the rotation angle between two adjacent layers. Our considered ideal patterns for the distribution of the interbead voids from 3D printing for the composite laminates with helicoidal and quasi-isotropic ($[0/\pm45/90]_{5\ s}$) stacking sequences are given in Figure 1C. However, in the actual printing process of the CF/PA6 filaments through the heated nozzle without any pressure mechanism in place, voids in the PA6 matrix and at the fiber-matrix interface, which could vary in size and spatial distributions, would appear because of the lack of matrix consolidation. Two groups of samples with different helicoidal angles were printed for static bending (group A) and Charpy impact tests (group B), respectively, together with their counterparts of quasi-isotropic stacking sequences in each group for comparison. The structural details of all printed samples are given in Table 1. X-ray computed tomography (CT) (Figure 1D) indicated that voids, marked in red, were distributed helicoidally, with the interbead voids concentrated in band-like areas parallel to the fiber orientation in each single layer. With the image in Figure 1E, the void fraction, calculated in terms of area fractions[25] for composites with a helicoidal angle of 16.36°, was measured to be ~7.1%. After hot pressing, the voids were almost eliminated, with the void fraction reduced to ~1.5% (Figure 1F).

Mechanical Properties

The load-displacement curves of printed specimens under three-point bending are shown in Figures 2A and 2B for helicoidal (group A-1) and quasi-isotropic (group A-2) samples, respectively. For the bioinspired helicoidal composites, the load-displacement curves in Figure 2A can be classified into four regions: an elastic region, a nonlinear region, a plateau region, and a failure region. The load increased nonlinearly following the initial elastic region; after reaching the peak load, the curves dropped sharply due to fiber breakage, which was apparent in the lower layers. Subsequently, cracks rapidly penetrated several layers in the thickness direction before being arrested. The helicoidal composites were observed to sustain the load (~150

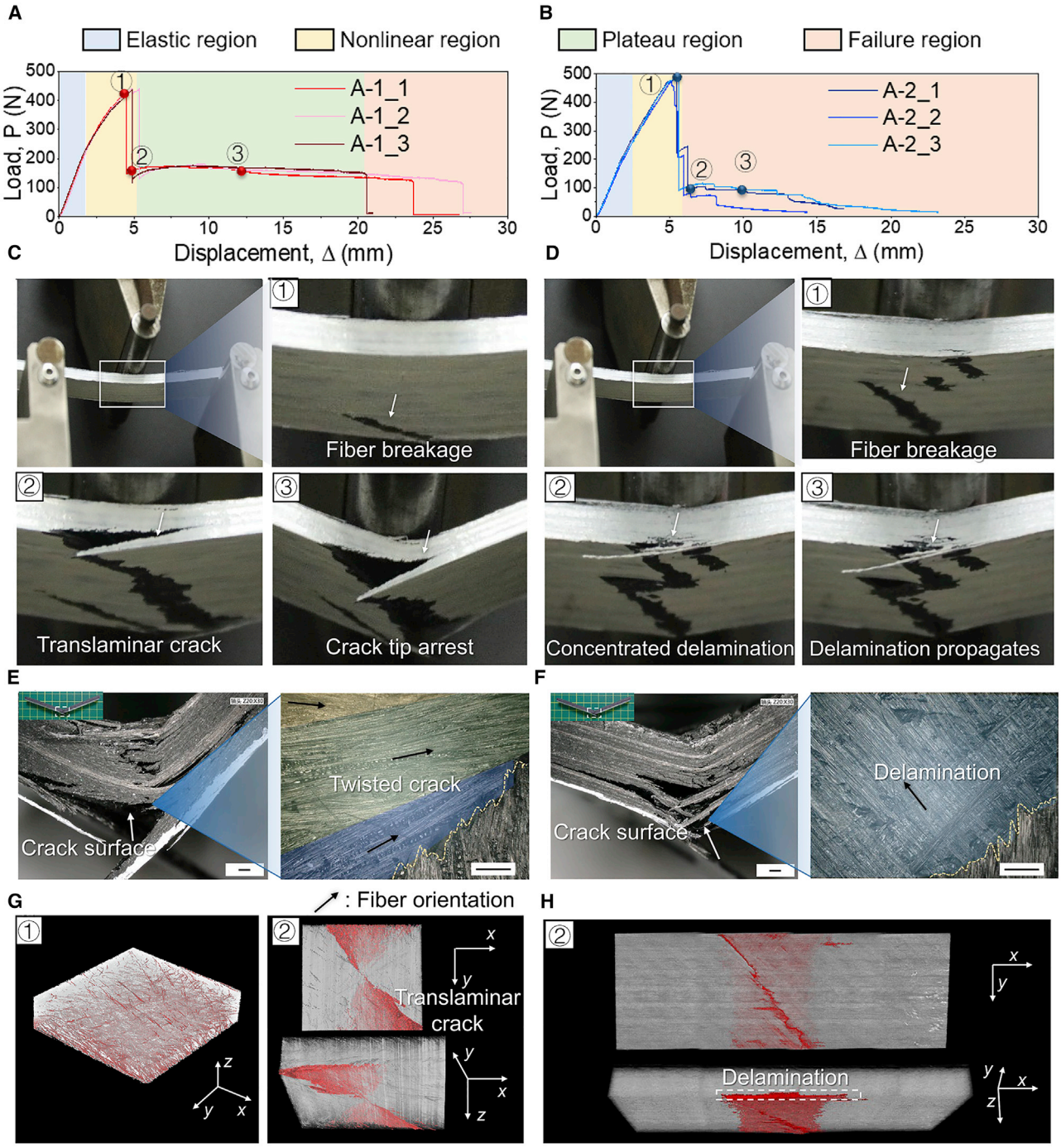

Figure 2. Three-Point Bending Tests

(A and B) Load-displacement curves for (A) helicoidal (A-1) and (B) quasi-isotropic (A-2) composite laminate samples under three-point bending.

(C and D) Corresponding deformation history accompanied by failure modes from the side view for (C) helicoidal (A-1) and (D) quasi-isotropic (A-2) samples, respectively.

(E and F) Micrograph observations for various crack morphologies for (E) helicoidal (A-1) and (F) quasi-isotropic (A-2) laminated samples after three-point bending tests.

(G and H) Micro-CT images for (G) helicoidal samples (A-1) from the nonlinear and failure regions and (H) quasi-isotropic samples (A-2) are presented with voids or crack paths highlighted in red.

The numbers in (C) and (G) correspond to those in (A), while those in (D) and (H) correspond to (B).

N) for a long period (~5–20 mm in displacement) before they fully collapsed, whereupon the cracks, which displayed a tortuous path, rapidly propagated through the sample thickness. Conversely, for the quasi-isotropic (group A-2) samples, three regions with no plateau region were observed in the load-displacement curves (Figure 2B). After the rapid load drop at the end of the nonlinear region, cracks again propagated rapidly through the thickness direction with extensive delamination. For these composites, the load-bearing capability in this failure region was diminished to essentially zero before abrupt failure.

Following testing, the fracture morphologies for different groups of samples were examined and images are shown in Figures 2E and 2F. In addition, detailed characterizations from computed X-ray micro-tomography (micro-CT) studies are also seen in Figures 2G and 2H, where the voids within the vicinity of the fracture regions are revealed in red. For the group A-1 helicoidal 16.36° composite laminates, while it was difficult to discern whether matrix cracking occurred in the nonlinear region owing to the ubiquitous presence of voids in the micro-CT images (Figure 2G), twisted crack trajectories and delaminations could be readily identified after the first load drop in Figures 2G and 2H, respectively.

The fracture modes after the Charpy pendulum tests are shown in Figure 3. For the 3D printed helicoidal composite laminates with and without hot pressing, twisted cracks were seen to be symmetrically distributed with respect to the neutral plane (Figures 3B and 3D), but the crack surface was much smaller, with brittle cracks in evidence after hot pressing. In contrast, extensive delaminations occurred in the quasi-isotropic samples (Figure 3C). A higher magnification of the Figure 3B image in Figure 3E provides more details of the nature of the twisted cracks in the helicoidal composites. Cracked layers on crack surfaces were divided by bands, where the fracture of interbead voids, sized in the range of tens of micrometers, was detected in the matrix. However, there were no such void bands on the twisted crack surfaces for the hot-pressed samples in group B-3 (Figure 3F). The ideal pattern for interbead void intervals between every two fiber bundles is shown in Figure 3G. A twisted crack in the helicoidal laminates penetrated each layer, with the crack front parallel to the fiber orientation in that layer. These observations suggest a specific role for the interbead voids to guide the tip of the twisting crack in the helicoidal composite laminates to form an ideally twisted crack trajectory, as shown by the white surface in Figure 3H. The lack of guidance from the interbead voids would result in crack growth with low energy absorption, including the brittle fracture with a non-ideal twisted crack path having a smaller surface area; this is typical of the helicoidal laminates after hot pressing, as the brown surface exhibits schematically in Figure 3H. However, more detailed effects on mechanical behavior, specifically due to the presence of the voids, from mere observations were difficult to discern; accordingly, to gain better comprehension of the contribution of the voids to the toughness, a relatively simple 2D FE model was developed, as discussed below.

The mechanical properties of the fabricated composite laminates were analyzed with void fraction variations based on the above experimental results, as shown in Figure 4A. The flexural stiffness E_f was defined in terms of the laminate width W and height H, as $E_f = (2D^3m/WH^3)$, where m is the slope of the load-displacement curve in the elastic region and D is the half-support span. The flexural strength was calculated by $\sigma_f = (3P_mD/WH^3)$ where P_m is the peak load at failure. Compared to their quasi-isotropic counterparts, the flexural stiffness E_f of the helicoidal 16.36° composites was >18% higher, but their flexural strength was 10% lower. The energy absorption U_b, measured by the area under the load-displacement curves until the

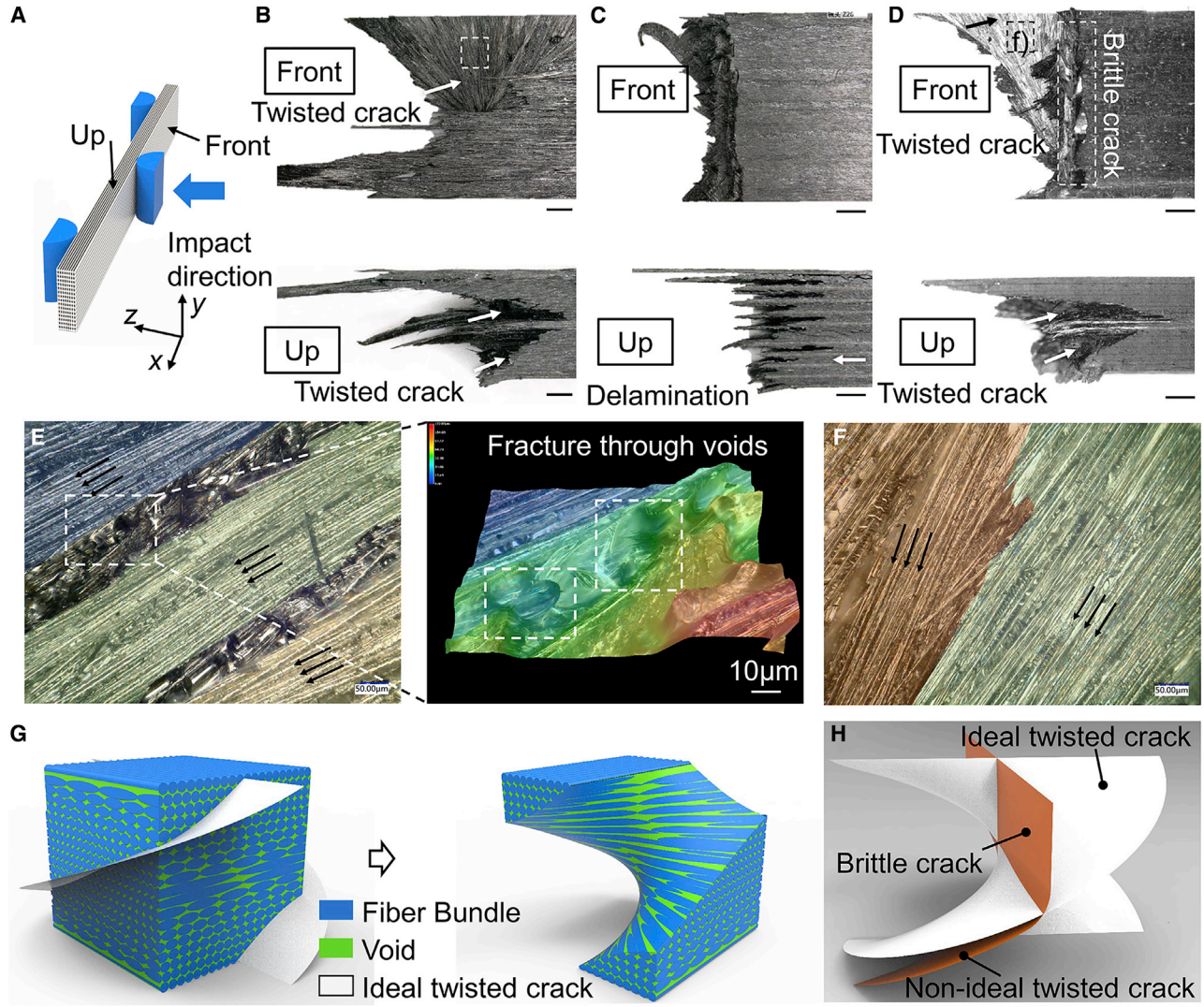

Figure 3. Charpy Impact Tests

(A–H) (A) Observation direction; fracture modes of (B) helicoidal 9.47° composite beams (group B-1), (C) quasi-isotropic composite beams (group B-2), and (D) helicoidal composite beams after hot pressing (group B-3) (scale bar: 100 μm); (E) microscopic observation of crack surface in (B), and fracture through voids; (F) microscopic observation of crack surface in (D); (G) geometric model of ideal twisted crack in a helicoidal composite with interbead voids and the exposed crack surface; and (H) a schematic comparison of crack paths in group B-1 and group B-3 (brown surface).

load dropped to 20% of the peak value, was used as an approximate estimate of the toughness (i.e., fracture resistance). Using these U_b measurements, the helicoidal 16.36° laminates were found to possess a toughness over a factor of 2 higher than that measured for the quasi-isotropic materials. Such an increased energy absorption of the helicoidal laminates was attributed to the unique twisting cracking mode that provided an extrinsic toughening mechanism (crack deflection or twist) to markedly diminish the crack-driving force (e.g., the strain energy release rate, stress intensity factor),[9,13] and therefore greatly minimize the risk of any fast-developing delamination. For the helicoidal composites with $\alpha = 36°$, a mixed-mode fracture was also observed with extensive twisted delamination cracks; the energy absorption of these composites was inferior to the helicoidal laminates with $\alpha = 16.36°$. The mechanisms for such fractures are analyzed in more detail below.

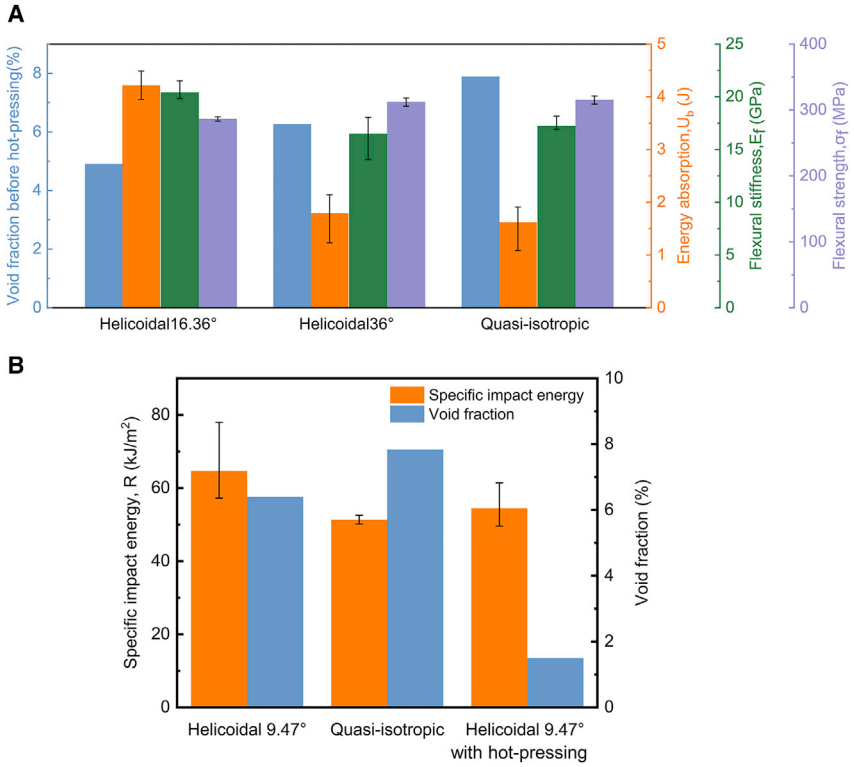

Figure 4. Comparison of Flexural and Impact Properties

(A) Comparisons of energy absorption, flexural stiffness, and flexural strength for helicoidal 16.36°, helicoidal 36°, and quasi-isotropic composite beams.

(B) Comparison of specific impact energy *R* between helicoidal and quasi-isotropic composite laminates.

Data are represented as median, maximum, and minimum values.

The impact properties of all of the samples were calculated in terms of the specific impact energy, $R = U_i/WH$, where U_i is the impact energy absorption. Values for the helicoidal laminated composites are compared with those of the quasi-isotropic laminates in Figure 4B. It is clear that 3D-printed helicoidal composites displayed >25% higher specific impact energy than their quasi-isotropic counterparts, provided that they were not hot pressed. With hot pressing, the specific impact energy *R* for group B-3 samples was decreased by 15.7% compared to group B-1 samples without hot pressing; in addition, the void fraction decreased from 7.1% to 1.5%. These results further confirm the role of voids in contributing to the impact fracture resistance of the helicoidal laminates by locally arresting the crack growth and facilitating the twisting patterns of crack paths, both serving to alleviate brittle fracture. We attempted to create voids in our composites induced by 3D printing to simulate those observed in certain biomaterials, for example, the mantis shrimp raptorial appendage, as we believed that the voids would contribute to the excellent impact resistance of these helicoidal constructions.

Interlaminar Stress Analysis

For engineering composite laminates, as failure can occur readily by ply delamination, interlaminar stress analysis is often used for their architectural design. To better understand these interlayer toughening mechanisms of Bouligand structures, the interlaminar stresses σ_{13}, σ_{23}, and σ_{33} between every 2 layers under 3-point bending were estimated using finite element analysis (FEA) for a helicoidal 16.36° composite

beam. (Note that 1–3 refers to the main directions in a single ply.) To validate the FEA used for interlaminar stress analysis, a 4-layer laminated composite $[0/90]_s$ was conducted, as depicted in Figure S1A. The loading method, geometry, mechanical properties of materials, and laminating schemes were the same as the finite differences (FD) model of Pipes and Pagano[26] and Solis et al.[27]. A minimum number of 6 FE nodes in the thickness direction of 1 layer was used. The FE model contained >1.6 million elements. The resultant stresses from those studies and the present work were compared and displayed good agreement, as shown in Figure S1B. In addition, a convergence study was ensured.

Subsequently, a one-quarter model consisting of linear hexahedral solid elements C3D8R in each layer was established with a locally refined mesh near the free edge *A″-A‴*, as shown in Figure 5A. Symmetrical boundary conditions and surface-to-surface contact were used to improve computational efficiency, with an imposed displacement of 1 mm. Using elastic parameters, specifically E_{11} = 137.9 GPa, $E_{22} = E_{33}$ = 14.5 GPa as elastic modulus, $\mu_{12} = \mu_{13} = \mu_{23}$ = 5.86 GPa as shear modulus, and $v_{12} = v_{13} = v_{23}$ = 0.21 as Poisson's ratio, taken from published work[21] for our calculations, the FE method was validated on a 4-layer laminate with a stacking sequence of [0/90/90/0] in tension by comparing the obtained interlaminar stress distributions with those in He et al.[21] Following validation, similar calculations were conducted on the composites with different laminating schemes. Interlaminar stress distributions for σ_{13}, σ_{23}, and σ_{33} in the area *A-A′-A″-A‴* (Figure 5A) were calculated, as shown in Figure 5B. Concentrated interlaminar tensile stresses σ_{33} can be found at the free edges (*A″-A‴*) of the helicoidal and quasi-isotropic composites, which would promote tensile opening and thus delamination at the free edge. However, interlaminar shear stresses σ_{13} and σ_{23} are also distributed widely along the interfaces (*y* direction), which can contribute to sudden shear-dominated delamination, as reported elsewhere.[28] For the helicoidal laminated composites, such σ_{13} and σ_{23} interlaminar shear stresses concentrate near the boundary area of the beam located between z/h = 2–5 in the lower half of the beam, and between z/h = 20–23 in the upper half. This could trigger the twisted crack formation in the area in between, as observed in Figure 2E. For the quasi-isotropic laminated composites, these interlaminar shear stresses are concentrated in multiple interfaces at z/h = 2, 6, 10 and symmetrically at z/h = 14, 18, 22, which implies that such delaminations could occur for the composite beam at all of these interfaces.

Theoretical Model

The fracture resistance of a composite laminate depends largely on its failure mode, specifically, if the crack is deflected at, or penetrates through, the laminae (or layered) regions. Accordingly, for the improved design of helicoidal composites, one approach is to relate the failure mode to the composite micro-architecture. To achieve this objective, we simplified the problem of crack propagation in 3D space as a plane-strain problem with crack growth in the symmetrical mid-plane along a path in the thickness direction (i.e., along the *y* direction). For the case of a crack penetrating the layers (Figure 6A), a homogeneous 2D beam model was established with an equivalent Young's modulus E_k for the k^{th} layer, where the crack is sited. Detailed calculations of E_k are provided below. For the case of a crack deflecting at the layers, the crack path is presumed to follow a straight line before encountering the interface, whereupon it deflects transversely along the interface, with a deflection length of *a* on either side. We establish here a bi-material beam model, shown in Figure 6B, which comprises two homogeneous layers with equivalent Young's moduli E_k and E_{k+1}, respectively. The equivalent Young's modulus, E_k,

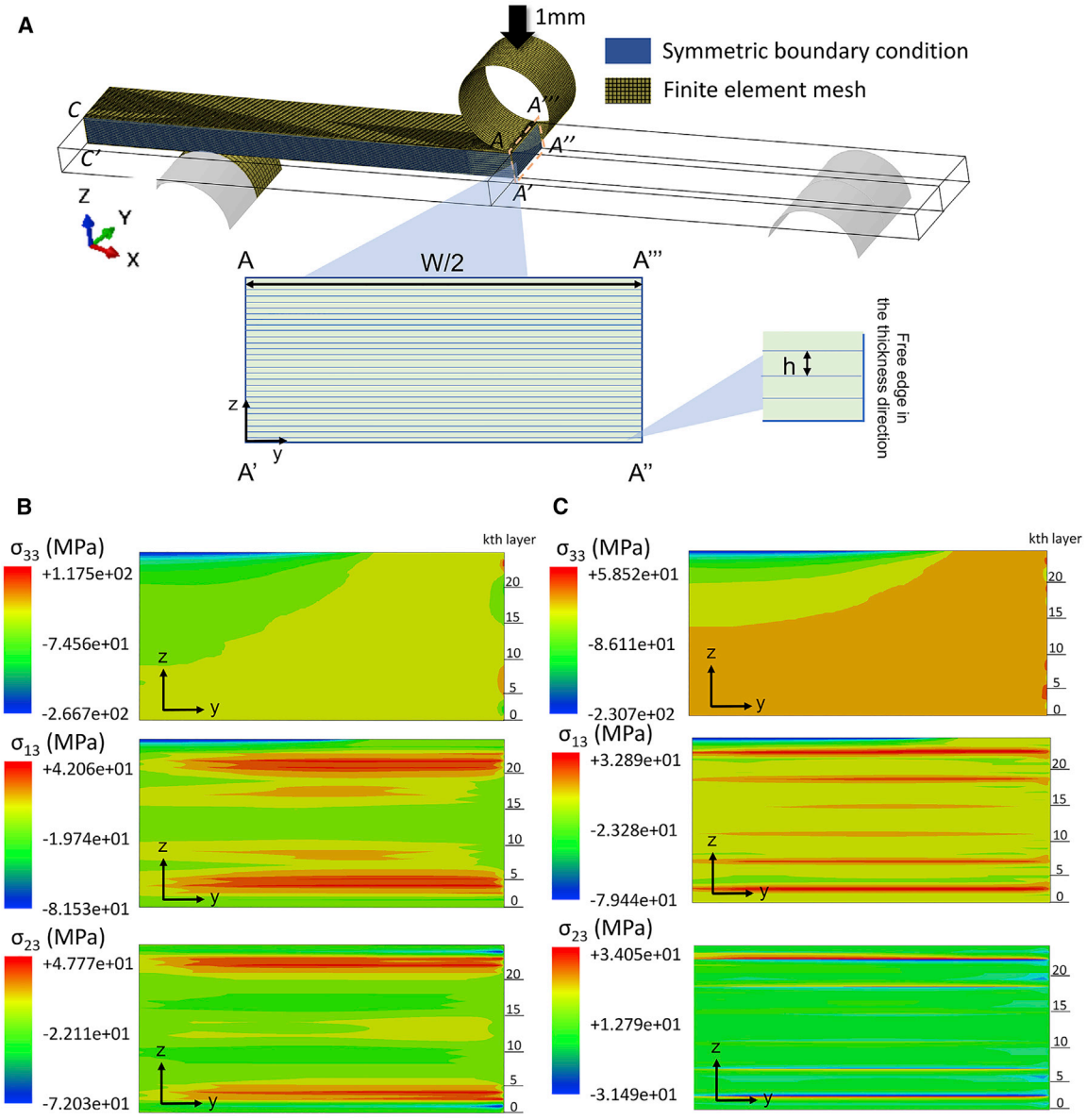

Figure 5. Interlaminar Stress Analysis Based on Finite Element Method

(A–C) (A) Finite element model. Interlaminar stresses distributions in the area *A*-*A*′- *A*″-*A*‴ for (B) helicoidal 16.36° composites and (C) quasi-isotropic composites: σ_{13}, σ_{23} and σ_{33} are the interlaminar stresses between 2 adjacent layers. Note that the number of the k^{th} layer is marked on the right side of the contours.

defined as the stiffness in the *x* direction, is analyzed for the subsequent stress calculations using the Euler-Bernoulli beam theory. According to Fischer et al.,[13] the equivalent Young's modulus varies continuously in the *z* direction and can be derived in Equations 1 and 2:

$$\tilde{E}_k = 2\overline{\Phi}(z)\varepsilon_z^2, \qquad \text{(Equation 1)}$$

$$\overline{\Phi}(\theta) = E_{22}\left(\tilde{\Phi}_1 + \tilde{\Phi}_2\cos^2\theta + \tilde{\Phi}_3\cos^4\theta\right) \Big/ \tilde{\Phi}_4, \qquad \text{(Equation 2)}$$

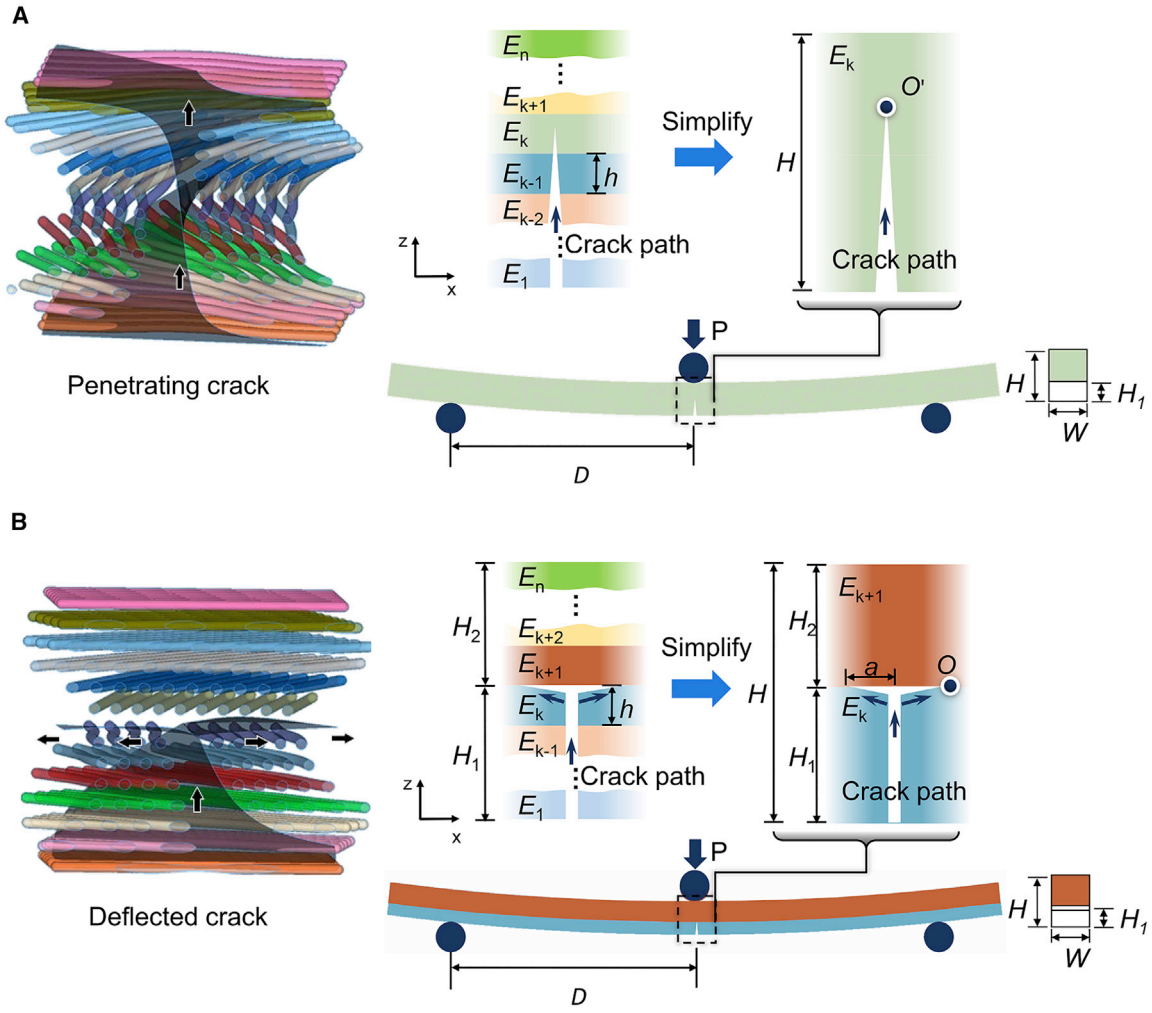

Figure 6. Simplification of Two Crack Propagation Scenarios
(A and B) Penetrating crack (A) and deflected crack (B).

where $\tilde{\Phi}_1 \sim \tilde{\Phi}_4$ are local elastic strain energy density items, which can be derived from expressions in the work of Fischer et al.[13] The 0° and 90° laminae have the highest and lowest values of their equivalent Young's modulus, respectively. Thus, the equivalent Young's modulus of the laminae with other orientations must vary between these maximum and minimum values.

For the crack deflected at the lamellae, the energy release rate G_D can be calculated based on Equation 3,[29] that is,

$$G_D = -\frac{P^2}{8W}\left(\frac{1}{\sum_c} - \frac{1}{\sum_{sub}}\right)(D-a)^2, \qquad \text{(Equation 3)}$$

where $\sum_{sub} = \frac{WH_2^3}{12} \times E_{sub}$, $\sum_c = I_c \times W \times E_c$, $I_c = \frac{H_1^3}{12} + \frac{\lambda H_2^3}{12} + \frac{\lambda H_1 H_2 (H_1 + H_2)^2}{4(H_1 + \lambda H_2)}$, $E_c = \frac{\tilde{E}_k \times H_1 + \tilde{E}_{k+1} \times H_2}{H}$, $\lambda = \frac{\tilde{E}_{k+1}}{\tilde{E}_k}$ and $E_{sub} = \tilde{E}_k$.

Here, H is laminate thickness, with H_1, H_2, and D defined in Figure 6.

For the crack penetrating the lamellae, the crack tip is assumed to be in pure mode I (tensile opening condition), with the corresponding energy release rate G_P calculated from Equation 4[30]:

$$G_p = \frac{K_1^2}{\tilde{E}_k}, \quad \text{(Equation 4)}$$

where the mode I stress intensity $K_1 = (3PD/2WH^{3/2}) f_1(H_1/H)$, P is the load in quasi-static three-point bending, and

$$f_1\left(\frac{H_1}{H}\right) = \frac{1.99 - \frac{H_1}{H}\left(1 - \frac{H_1}{H}\right)\left(2.15 - 3.93\frac{H_1}{H} + 2.7\left(\frac{H_1}{H}\right)^2\right)}{\left(1 + 2\frac{H_1}{H}\right)\left(1 - \frac{H_1}{H}\right)^{3/2}}.$$

Following the original idea of Gurney and Hunt[31] that a crack will propagate in the direction of the lowest load, equivalent to maximizing the entropy increase of an isothermal system, Cherry and Harrison[32] derived a general criterion for cracking (penetrating) or splitting (deflecting) in an anisotropic medium (or bi-material), which was also considered by Atkins and Mai.[33] He and Hutchinson[34] later obtained the same criterion to determine whether the crack would penetrate through or deflect into the interface. These conditions are:

$$\begin{cases} \frac{G_P}{G_D} > \frac{G_{PC}}{G_{DC}} & \textit{Penetrating crack} \\ \frac{G_P}{G_D} < \frac{G_{PC}}{G_{DC}} & \textit{Deflected crack} \end{cases}. \quad \text{(Equation 5)}$$

G_{PC} and G_{DC} are fracture toughness values of the lamella and interface, which can be determined based on mode I and mode II fracture tests. As given in Equation 5, if the ratio G_P:G_D drops below the fracture toughness ratio G_{PC}:G_{DC}, a delamination crack occurs at the corresponding position in the z direction. The opposite is true if G_P:G_D is larger than G_{PC}:G_{DC}, whereupon the crack will penetrate the interface.

G_{PC} and G_{DC} were calculated from the following expressions:

$$G_{PC} = \frac{2P_{max,1}D}{BL^{3/2}} \bullet 3\sqrt{\frac{a}{L}} \bullet \frac{1.99 - \left(\frac{a}{L}\right)\left(1 - \frac{a}{L}\right)\left[2.15 - 3.93\frac{a}{L} + 2.7\left(\frac{a}{L}\right)^2\right]}{2\left(1 + 2\frac{a}{L}\right)\left(1 - \frac{a}{L}\right)^{3/2}}, \quad \text{(Equation 6)}$$

$$G_{DC} = \frac{9P_{max,II}{}^2 a^2}{16E_{11}B^2H^3}, \quad \text{(Equation 7)}$$

where L, B, D, and H are the length, width, half-span, and height of the samples, and a is the length of the notched crack. $P_{max,I}$ and $P_{max,II}$ refer to the peak load values in the mode I and mode II tests, as shown in Figures S2C and S2D, respectively. The tested values of G_{PC} and G_{DC} were 462.3 N•m^{-1} and 755.8 N•m^{-1}, respectively. Values of the Young's modulus along and perpendicular to the fiber orientation for unidirectional CF/nylon composite laminates were calibrated through comparison between FEA and experimental results, yielding E_{11} = 52 GPa, E_{22} = E_{33} = 2.334 GPa, μ_{12} = μ_{13} = μ_{23} = 10.4 GPa, and v_{12} = v_{13} = v_{23} = 0.25.

For the helicoidal 16.36° composites, the G_P/G_D curves lie above the critical value G_{PC}/G_{DC}; therefore, a penetrating or a twisted crack is the only expected cracking configuration. However, the relatively higher G_P/G_D values around the valley

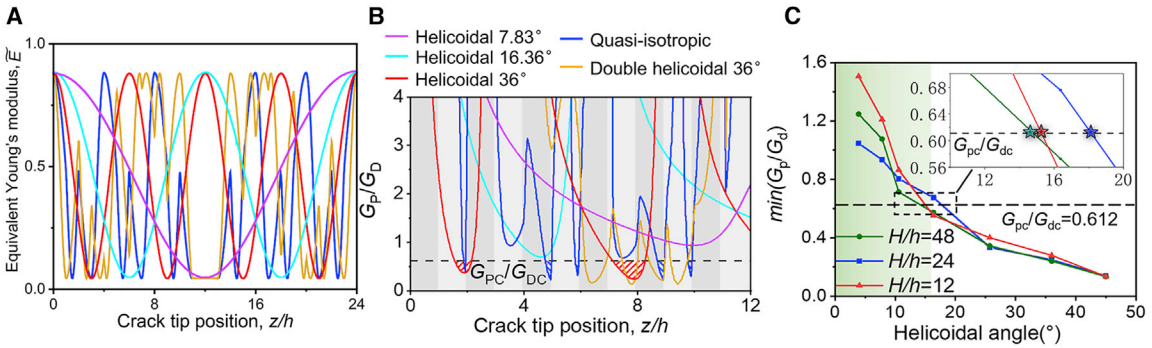

Figure 7. Mechanical Properties of the Composites

(A) Equivalent Young's modulus in thickness direction for helicoidal 7.83°, helicoidal 16.36°, helicoidal 36°, double helicoidal 36°, and quasi-isotropic composite beams.

(B) Variation in G_P/G_D with position of crack tip in the thickness direction for the lamination configuration schemes above. Predicted delamination positions are shown in shaded areas.

(C) The critical angle for the crack mode transitioning from penetrating the layers to delaminating at the matrix-layer interfaces for the helicoidal laminated composite, with H/h ranging from 12 to 48.

between z/h = 2–5 also indicate those locations where delaminations can occur easily due to the high interlaminar shear stress simulation results (Figure 5B). As revealed by the shaded areas below the critical G_{PC}/G_{DC} (= 0.612) line (Figure 7B), delamination cracks can initiate in the thickness direction twice in the helicoidal 36° composites; however, deflections will occur >5 times in the quasi-isotropic composites. These results agree well with experimental observations. For the quasi-isotropic composites, the "valleys" located at z/h = 2, 6, and 10 are consistent with the interlaminar shear stress simulation results (Figure 5C).

Based on the above theoretical model, fracture modes are compared (Figure 7B) for composites with various lamellar stacking schemes with a fixed 24 layers. These include helicoidal composites with α = 7.83°, α = 36°, and double helicoidal composites with α = 36° (i.e., stacking sequence $[0/90/36/126/\ldots/180/90]_s$) inspired by the microstructures of the scales of coelacanth fish.[35] Only half of the samples in the thickness direction (i.e., the first 12 layers) was considered in each case. Among the 5 laminating schemes, delamination is only not likely to occur in the helicoidal 7.83° and 16.36° composites. The double helicoidal 36° does not exhibit delamination until the crack penetrates through one-third of the full thickness. In contrast, the quasi-isotropic composites always exhibit the maximum quantity of delamination cracks. In addition, the effect of the helicoidal angle α on the cracking mode, depicted in Figure 7C, shows that there is a critical angle of α_c = 18.2°, for a major change in the fracture configuration at H/h = 24. Helicoidal laminates with $\alpha < \alpha_c$ are not likely to suffer delamination; however, based on an investigation of the effect of non-dimensional layer thickness, H/h (Figure 7C), this has little effect on whether delamination occurs (i.e., the value of α_c is essentially unaffected by the thickness of the layers).

Toughening Mechanism of Voided Composites

To further examine the toughening effect of voids, we considered for simplicity unidirectional fiber reinforced composite samples with matrix voids. 2D FE models were constructed under compact-tension loading to compare the deformation behavior of the composites with and without voids. The load was applied either perpendicular or parallel to the fibers with a crack in the matrix as shown in Figure 8A. The matrix crack propagates in the voided system perpendicular to the fibers (in case I) or

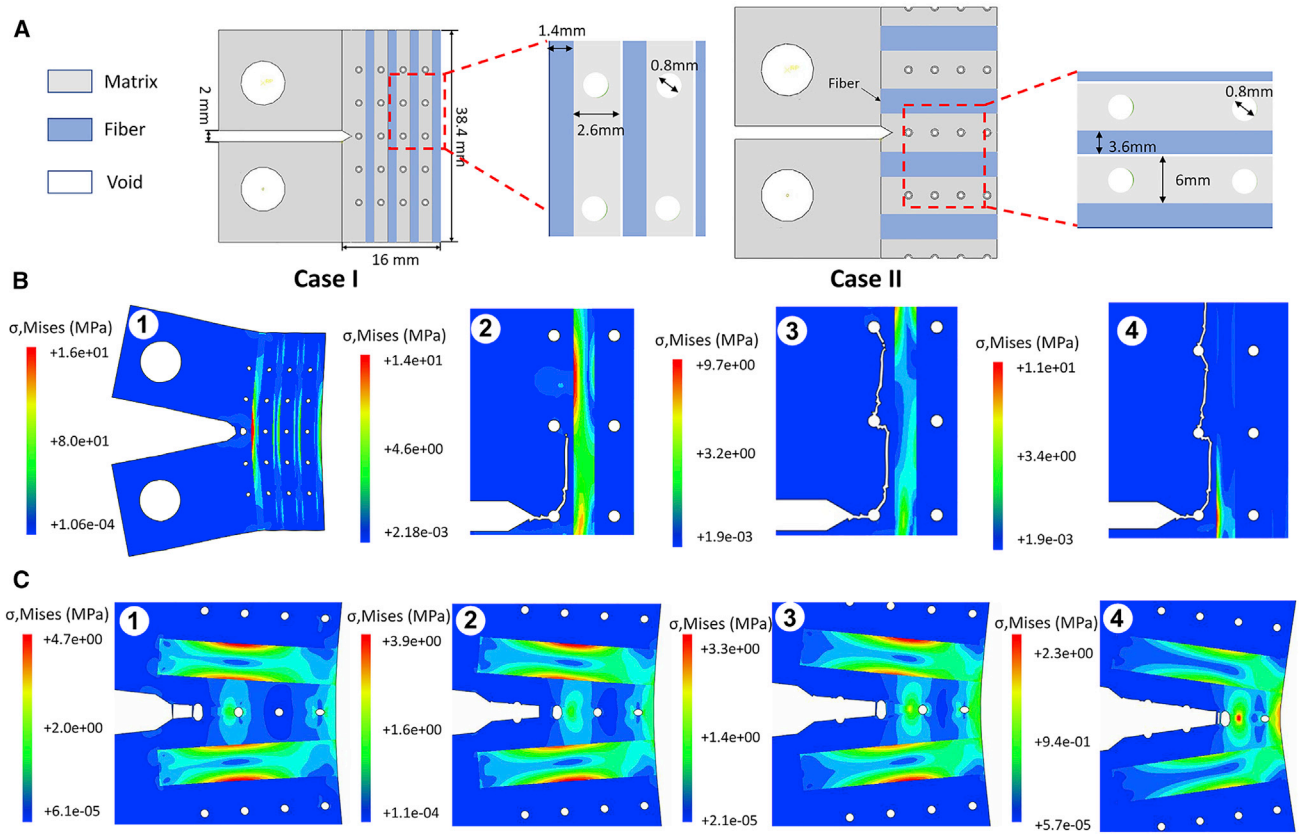

Figure 8. Finite Element Modeling of Toughening Mechanisms for Voids in a Fiber Composite

(A–C) Two cases are shown for a matrix crack propagating in a composite containing voids (A). Variations in stress contours as the matrix crack propagates, (B) perpendicular to the fibers (case I), and (C) parallel to the fibers, with the voids between them (case II).

parallel to the fibers with the voids between them (in case II). The stress contour variations during crack advance are shown in Figures 8B and 8C. In case I, the crack propagates toward the first fiber-matrix interface but deflects as the crack tip reaches the first void and follows a path through the adjacent voids (Figure 8B). In case II, the crack runs between two fibers and propagates through each void; voids close to the crack tip expand and tend to coalesce, which triggers plastic deformation in the surrounding matrix. Accordingly, we can conclude that the collapse of micrometer-sized voids and associated microcracking before the main twist fracture will contribute to the impact resistance of the composite.

In conclusion, in this study, we have focused on unraveling the underlying mechanisms that have perhaps been overlooked in previous research,[6,13] and as such, we have attempted to develop, using 3D printing, bioinspired impact-resistant continuous CF-reinforced composite laminate materials in the image of the structure of these dactyl clubs. A summary of our principal conclusions follows:

In addition to their Bouligand architecture, which is the most characteristic feature of these biomaterials, voids were observed between polysaccharide α-chitin and protein interfaces in the dactyl club of *O. japonicas* as one species of aggressive mantis shrimp. Accordingly, helicoidal laminated composites were designed and fabricated by continuous-fiber 3D printing technology to mimic the periodic region of the dactyl club, with the presence of interbead voids

distributed helicoidally. As seen in micro-CT imaging, the voids were concentrated in band-like areas parallel to fiber orientation in each single layer.

During static bending, our 3D-printed helicoidal laminates were seen to be capable of still carrying loads after significant damage initiation and accumulation; this manifested as a prolonged plateau in stress in their stress-strain curves associated mechanistically with highly deflected, twisted cracks penetrating through the thickness of the material. By comparison, corresponding quasi-isotropic composite laminates fabricated from the same materials, but without the Bouligand structure, failed abruptly, with significant delaminations between the layers. The high specific impact energy of 3D-printed helicoidal composites was largely lost after the laminates were subsequently hot pressed, which served to eliminate the presence of the interbead voids. This result indicates the important contribution of voids in generating impact toughness.

The interlaminar stress in the synthetic helicoidal composites was studied by the FE method and compared with that of the quasi-isotropic counterparts to explain why the helicoidal composites with their Bouligand architecture were highly resistant to interface delamination. Meanwhile, a theoretical model, based on a plane-strain hypothesis, was used to correlate the interply angle with possible crack configurations, specifically to discern whether a crack incident on the layers would penetrate them (as a twisted crack) or be locally arrested, causing delamination along the matrix-layer interface. Such considerations were used to select the optimal laminating scheme for fracture resistance.

To examine the toughening effect of the voids, unidirectional fiber-reinforced composites containing matrix voids were modeled using finite-element analysis. The voids were found to deform or to coalesce when the matrix crack propagated perpendicular to the fibers or parallel to the fibers, with the voids between them. Accordingly, we believe that the voids in the present study, which were introduced by a lack of consolidation during printing, can contribute to toughness by void collapse and associated microcracking. The presence of the voids also serves to guide the fracture in the formation of an ideally twisted crack, which acts to enhance the impact energy absorption of the helicoidal composites extrinsically by reducing the near-tip crack-driving force through crack deflection or twisting mechanisms.

EXPERIMENTAL PROCEDURES

Resource Availability

Lead Contact

Further information and requests for resources and reagents should be directed to the Lead Contact, Sha Yin (shayin@buaa.edu.cn).

Materials Availability

Commercially available CF-reinforced nylon filaments were purchased directly from Markforged. All of the filaments were printed directly without treatment.

Data and Software Availability

The authors declare that data supporting the findings of this study are available within the article and the Supplemental Information.

3D Printing

Our bioinspired composite laminates were fabricated using a Markforged Mark Two 3D printer with pre-impregnated continuous CF/nylon (PA6) filament. In the FDM process, the CF/PA6 filament was fused in the nozzle, extruded out, oriented along the designed direction, and then solidified to form one unidirectional layer. After

repeating layer by layer, the bioinspired composites with a designed helicoidal stacking sequence (e.g., $[0/16.36/32.72.../163.6/180]_s$) with helicoidal angle α = 16.36° and 24 fiber layers, were finally formed. Here, we generally call the fiber orientation in the first layer the baseline and zero direction, and the second layer rotated α, and the third layer another α until completing all of the lay-ups, according to that illustrated in the square brackets. Note that the accuracy of the geometrical dimensions and fiber orientation is best achieved with the automatic printing procedures used here instead of traditional manual lay-ups. Notched samples were also printed similarly for toughness testing. The dimensions and fiber orientation were shown in Figures S2A and S2B.

Hot Pressing

Following He et al.,[21] we further treated our 3D-printed samples with hot pressing at 230°C and 2 MPa pressure in line as the common processing method for engineering composites, to eliminate voids in the printed samples for comparison.

Microstructure and Failure Characterization

The structural architecture of the appendages of the dactyl club was examined with an Olympus OLS5000 laser scanning microscope. Detailed features were additionally observed by scanning electron microscopy using a Hitachi S-4800 SEM. The printed composites were also examined with X-ray CT using a Zeiss Xradia 410 Versa system. The failure modes for different groups of samples were observed in a Keyence VHX-6000 optical microscope.

Quasi-static Three-Point Bending Tests

Quasi-static three-point bending tests were performed on printed specimens in group A to examine their mechanical properties, as shown in Figure 2A. In accordance with ASTM Standard D7264/D7264M,[36] the overall dimensions of the bending samples were 96 × 13 × 3.5 mm, with a span-to-thickness ratio of 20:1. An Instron 8801 electro servo-hydraulic testing machine was used for the bending tests using a displacement rate of 1 $mm \cdot min^{-1}$. At least three repeated tests for each type of specimen were performed to ensure repeatability.

Charpy Impact Tests

To evaluate the dynamic impact resistance, Charpy pendulum tests were performed flatwise on unnotched beams with an input energy of 15 J (at an initial impact velocity of 3.81 $m \cdot s^{-1}$) using a Zwick/Roell Charpy tester; a loading span of 62 mm was used, based on British Standard BS EN ISO 179-2.[37] Only group B-3 samples were treated by hot pressing. At least five repeated tests for each kind of specimen were conducted to ensure repeatability.

Fracture Toughness Tests

Fracture toughness tests were performed on an Instron 8801 universal mechanical testing machine at a displacement rate of 0.5 $mm \cdot min^{-1}$. Single-edge notch bend (SENB) and end-notched flexure (ENF) samples were, respectively, used for measurements of the respective mode I and II fracture toughness values G_{PC} and G_{DC}.

Toughening Mechanism Modeling

To examine the toughening effect of voids, unidirectional fiber-reinforced composite samples with spherical matrix voids were modeled in ABAQUS with a 2D plane strain condition for simplicity. Compact-tension (C(T)) samples with and without voids were generated with geometries according to ASTM Standard D5045 for fracture toughness testing.[38] A matrix crack, 2 mm wide and tip chamfer angle 30°, was

induced to propagate into a unidirectional fiber and voided matrix composite system perpendicular to the fibers (case I) or parallel to the fibers, with the voids between them (case II). In case I, the diameter of fibers was set at 1.4 mm; in case II, it was set at 3.6 mm, with a constant fiber fraction of 35%. Matrix voids with a diameter of 0.8 mm were assumed to be uniformly distributed, with a void fraction of 7%, which was the same as the value of the void fraction in the printed samples. A linear tetrahedral element, CPS4R, was used, with the materials parameters summarized in Table S1. The mesh size was refined to be 0.2 mm in the crack propagation zone and 0.4 mm in the other areas, with the overall element number of 26,164 for the 2 types of meshed samples shown in Figure S3. All of the samples were loaded at a displacement rate of 10 mm•min^{-1}.

SUPPLEMENTAL INFORMATION

Supplemental Information can be found online at https://doi.org/10.1016/j.xcrp.2020.100109.

ACKNOWLEDGMENTS

This work was supported by the Open Research Fund Project of the State Key Laboratory of Advanced Forming Technology & Equipment (SKL2019001), the Young Elite Scientist Sponsorship Program by the China Association for Science and Technology (CAST), the National Key Research and Development Program of China (2017YFB0103703), and the Fundamental Research Funds for the Central Universities, Beihang University.

AUTHOR CONTRIBUTIONS

S.Y., Q.H., and H.C. fabricated all of the composites, H.C. and R.Y. carried out the mechanical testing, H.C. and D.C. performed the microscopy and computed tomography, H.C. developed the theoretical fracture model, and R.Y. carried out the simulation of the voided composites, all under the supervision of S.Y., J.X., L.Y., Y.-W.M., and R.O.R. S.Y., J.X., and R.O.R. wrote the manuscript with assistance from all of the authors.

DECLARATION OF INTERESTS

The authors declare no competing interests.

Received: March 23, 2020
Revised: May 15, 2020
Accepted: June 4, 2020
Published: July 15, 2020

REFERENCES

1. Meyers, M.A., Chen, P.Y., Lin, A.Y.M., and Seki, Y. (2008). Biological materials: structure and mechanical properties. Prog. Mater. Sci. *53*, 1–206.

2. Liu, Z., Zhang, Z., and Ritchie, R.O. (2018). On the materials science of Nature's arms race. Adv. Mater. *30*, e1705220.

3. Patek, S.N., Korff, W.L., and Caldwell, R.L. (2004). Biomechanics: deadly strike mechanism of a mantis shrimp. Nature *428*, 819–820.

4. Yaraghi, N.A., Guarín-Zapata, N., Grunenfelder, L.K., Hintsala, E., Bhowmick, S., Hiller, J.M., Betts, M., Principe, E.L., Jung, J.Y., Sheppard, L., et al. (2016). A sinusoidally architected helicoidal biocomposite. Adv. Mater. *28*, 6835–6844.

5. Amini, S., Tadayon, M., Idapalapati, S., and Miserez, A. (2015). The role of quasi-plasticity in the extreme contact damage tolerance of the stomatopod dactyl club. Nat. Mater. *14*, 943–950.

6. Grunenfelder, L.K., Milliron, G., Herrera, S., Gallana, I., Yaraghi, N., Hughes, N., Evans-Lutterodt, K., Zavattieri, P., and Kisailus, D. (2018). Ecologically driven ultrastructural and hydrodynamic designs in stomatopod cuticles. Adv. Mater. *30*, 1705295.

7. Weaver, J.C., Milliron, G.W., Miserez, A., Evans-Lutterodt, K., Herrera, S., Gallana, I., Mershon, W.J., Swanson, B., Zavattieri, P., DiMasi, E., and Kisailus, D. (2012). The stomatopod dactyl club: a formidable damage-tolerant biological hammer. Science *336*, 1275–1280.

8. Yaraghi, N.A., and Kisailus, D. (2018). Biomimetic structural materials: inspiration from design and assembly. Annu. Rev. Phys. Chem. *69*, 23–57.

9. Suksangpanya, N., Yaraghi, N.A., Kisailus, D., and Zavattieri, P. (2017). Twisting cracks in

Bouligand structures. J. Mech. Behav. Biomed. Mater. *76*, 38–57.

10. Grunenfelder, L.K., Suksangpanya, N., Salinas, C., Milliron, G., Yaraghi, N., Herrera, S., Evans-Lutterodt, K., Nutt, S.R., Zavattieri, P., and Kisailus, D. (2014). Bio-inspired impact-resistant composites. Acta Biomater. *10*, 3997–4008.

11. Suksangpanya, N., Yaraghi, N.A., Pipes, R.B., Kisailus, D., and Zavattieri, P. (2018). Crack twisting and toughening strategies in Bouligand architectures. Int. J. Solids Struct. *150*, 83–106.

12. Song, Z., Ni, Y., and Cai, S. (2019). Fracture modes and hybrid toughening mechanisms in oscillated/twisted plywood structure. Acta Biomater. *91*, 284–293.

13. Fischer, F.D., Kolednik, O., Predan, J., Razi, H., and Fratzl, P. (2017). Crack driving force in twisted plywood structures. Acta Biomater. *55*, 349–359.

14. San Ha, N., and Lu, G. (2019). A review of recent research on bio-inspired structures and materials for energy absorption applications. Compos. Part B Eng. *181*, 107496.

15. Moini, M., Olek, J., Youngblood, J.P., Magee, B., and Zavattieri, P.D. (2018). Additive manufacturing and performance of architectured cement-based materials. Adv. Mater. *30*, e1802123.

16. Gantenbein, S., Masania, K., Woigk, W., Sesseg, J.P.W., Tervoort, T.A., and Studart, A.R. (2018). Three-dimensional printing of hierarchical liquid-crystal-polymer structures. Nature *561*, 226–230.

17. Yang, Y., Chen, Z., Song, X., Zhang, Z., Zhang, J., Shung, K.K., Zhou, Q., and Chen, Y. (2017). Biomimetic anisotropic reinforcement architectures by electrically assisted nanocomposite 3D printing. Adv. Mater. *29*, 1605750.

18. Ribbans, B., Li, Y., and Tan, T. (2016). A bioinspired study on the interlaminar shear resistance of helicoidal fiber structures. J. Mech. Behav. Biomed. Mater. *56*, 57–67.

19. Mencattelli, L., and Pinho, S.T. (2019). Realising bio-inspired impact damage-tolerant thin-ply CFRP Bouligand structures via promoting diffused sub-critical helicoidal damage. Compos. Sci. Technol. *182*, 107684.

20. Blok, L.G., Longana, M.L., Yu, H., and Woods, B.K. (2018). An investigation into 3D printing of fibre reinforced thermoplastic composites. Addit. Manuf. *22*, 176–186.

21. He, Q., Wang, H., Fu, K., and Ye, L. (2020). 3D printed continuous CF/PA6 composites: effects of microscopic voids on mechanical performance. Compos. Sci. Technol. *191*, 108077.

22. Mehdikhani, M., Gorbatikh, L., Verpoest, I., and Lomov, S.V. (2019). Voids in fiber-reinforced polymer composites: a review on their formation, characteristics, and effects on mechanical performance. J. Compos. Mater. *53*, 1579–1669.

23. Dasari, A., Yu, Z.Z., and Mai, Y.-W. (2007). Trans-crystalline regions in the vicinity of nano-fillers in polyamide-6. Macromolecules *40*, 123–130.

24. Dasari, A., Zhang, Q.X., Yu, Z.Z., and Mai, Y.-W. (2010). Toughening polypropylene and its nanocomposites with submicrometer voids. Macromolecules *43*, 5734–5739.

25. Purslow, D. (1984). On the optical assessment of the void content in composite materials. Composites *15*, 207–210.

26. Pipes, R.B., and Pagano, N.J. (1970). Interlaminar stresses in composite laminates under uniform axial extension. J. Compos. Mater. *4*, 538–548.

27. Solis, A., Sánchez-Sáez, S., and Barbero, E. (2018). Influence of ply orientation on free-edge effects in laminates subjected to in-plane loads. Compos. Part B Eng. *153*, 149–158.

28. Sun, C.T., and Chu, G.D. (1991). Reducing free edge effect on laminate strength by edge modification. J. Compos. Mater. *25*, 142–161.

29. Qu, D., Gaganidze, E., Vaßen, R., and Aktaa, J. (2018). Determination of interface toughness of functionally graded tungsten/EUROFER multilayer at 550 °C by analytical and experimental methods. Eng. Fract. Mech. *202*, 487–499.

30. Nobile, L. (2000). Mixed mode crack initiation and direction in beams with edge crack. Theor. Appl. Fract. Mech. *33*, 107–116.

31. Gurney, C., and Hunt, J. (1967). Quasi-static crack propagation. Proc. Roy. Soc. A Math. Phys. Sci. *A299*, 508–524.

32. Cherry, B.W., and Harrison, N.L. (1970). Crack propagation directions in anisotropic media. Fibre Sci. Technol. *2*, 299–301.

33. Atkins, A.G., and Mai, Y.-W. (1985). Elastic and Plastic Fracture (Ellis Horwood).

34. He, M., and Hutchinson, J.W. (1989). Crack deflection at an interface between dissimilar elastic materials. Int. J. Solids Struct. *25*, 1053–1067.

35. Quan, H., Yang, W., Schaible, E., Ritchie, R.O., and Meyers, M.A. (2018). Novel defense mechanisms in the armor of the scales of the "living fossil" coelacanth fish. Adv. Funct. Mater. *28*, 1804237.

36. ASTM. D7264/D7264M. ASTM standard test method for flexural properties of polymer matrix composite materials. https://www.astm.org/Standards/D7264.

37. British Standards Institute. BS EN ISO 179-2 Plastics. Determination of Charpy impact properties. Part 2. Instrumented impact test. https://www.iso.org/obp/ui/#iso:std:iso:179:-2:ed-2:v1:en.

38. ASTM. ASTM D5045 - 14. Standard test methods for plane-strain fracture toughness and strain energy release rate of plastic materials. https://www.astm.org/Standards/D5045.htm.